

## Article

# Axial Motion Characterization of a Helical Ionic Polymer Metal Composite Actuator and Its Application in 3-DOF Micro-Parallel Platforms

Yuwei Wu <sup>1</sup>, Min Yu <sup>1,\*</sup>, Qingsong He <sup>1,\*</sup>, David Vokoun <sup>2</sup>, Guoxiao Yin <sup>1</sup>, Xianrui Xu <sup>1</sup> and Pengfei Lyu <sup>3</sup>

<sup>1</sup> College of Mechanical and Electrical Engineering, Nanjing University of Aeronautics and Astronautics, Nanjing 210016, China; wyw826@nuaa.edu.cn (Y.W.); yinguoxiao@nuaa.edu.cn (G.Y.); xianrui@nuaa.edu.cn (X.X.)

<sup>2</sup> Institute of Physics of the ASCR, 182 21 Prague, Czech Republic; vokoun@fzu.cz

<sup>3</sup> College of Energy and Power Engineering, Nanjing University of Aeronautics and Astronautics, Nanjing 210016, China; lvpengfei@nuaa.edu.cn

\* Correspondence: yumin@nuaa.edu.cn (M.Y.); heqingsong@nuaa.edu.cn (Q.H.)

**Abstract:** In this work, a helical ionic polymer metal composite (IPMC) was fabricated by thermal treatment in a mold with helix grooves. The axial actuation behaviors of the helical IPMC actuator were observed, and the electromechanical and electrochemical characteristics were evaluated. The experimental results showed that as the voltage increased and the frequency decreased, the axial displacement, axial force, and electric current of the actuator all increased. Compared with square wave and sinusoidal signals, the actuator exhibited the most satisfactory motion under the direct current (DC) signal. For the electrochemical test, as the scanning rate decreased, the gravimetric specific capacitance increased. Within a suitable voltage range, the actuator was chemically stable. In addition, we coupled the Electrostatics module, Transport of Diluted Species module, and Solid Mechanics module in COMSOL Multiphysics software to model and analyze the helical IPMC actuator. The simulation data obtained were in good agreement with the experimental data. Finally, by using three helical IPMC actuators as driving components, an innovative three-degree-of-freedom (3-DOF) micro-parallel platform was designed, and it could realize a complex coupling movement of pitch, roll, and yaw under the action of an electric field. This platform is expected to be used in micro-assembly, flexible robots, and other fields.

**Keywords:** IPMC; helical; actuation performance; model; multiphysics; 3-DOF platform



**Citation:** Wu, Y.; Yu, M.; He, Q.; Vokoun, D.; Yin, G.; Xu, X.; Lyu, P. Axial Motion Characterization of a Helical Ionic Polymer Metal Composite Actuator and Its Application in 3-DOF Micro-Parallel Platforms. *Actuators* **2021**, *10*, 248. <https://doi.org/10.3390/act10100248>

Academic Editors: Jaehwan Kim, Hyun Chan Kim and Sungryul Yun

Received: 31 August 2021

Accepted: 23 September 2021

Published: 27 September 2021

**Publisher's Note:** MDPI stays neutral with regard to jurisdictional claims in published maps and institutional affiliations.



**Copyright:** © 2021 by the authors. Licensee MDPI, Basel, Switzerland. This article is an open access article distributed under the terms and conditions of the Creative Commons Attribution (CC BY) license (<https://creativecommons.org/licenses/by/4.0/>).

## 1. Introduction

In recent years, the rapid development of precision positioning technology has promoted a large number of applications of multi-degree-of-freedom (multi-DOF) motion platforms in fields such as optical microscopes [1,2], micro-assembly stations [3], and micro-robots [4–6]. Multi-DOF platforms are usually classified into two typical system configurations, serial and parallel [7]. The serial configuration adopts a stacked or nested structure, which has the advantage of independent motion decoupling. However, it also has some shortcomings, for example, different axes have different dynamic characteristics, and positioning errors produced by each axis will accumulate [8], leading to a decline in accuracy. For the parallel configuration, the inertia is small, and the closed-loop kinematic chains enable multi-DOF platforms to achieve high rigidity, carrying capacity, and accuracy [9]. Therefore, the parallel configuration is more popular than the serial one. At present, piezoelectric actuators [10–13], electromagnetic actuators [14–16], and magnetostrictive actuators [17–19] are used as the driving components of multi-DOF micro-parallel platforms. However, the platforms driven by these actuators suffer from the defects of complex structure and high power consumption. Hence, it is a current challenge to

develop a brand-new multi-DOF motion platform using smart material actuators with excellent performance.

Among the large family of smart materials, the ionic polymer metal composite (IPMC) is an electroactive material, which has become a research hotspot [20–25] due to its low voltage, large deformation, simple structure, light weight [26], and rapid response. For a helical-shaped IPMC, Kim and Shahinpoor [27] first proposed that it can function as a linear actuator. Subsequently, Li et al. [28] investigated its radial actuation performance and applied it to biomedical active stents.

In this work, more attention was paid to the axial actuation performance of the helical IPMC actuator. Furthermore, a novel type of three-degree-of-freedom (3-DOF) micro-parallel motion platform was developed by innovatively using three helical IPMC actuators as its driving components. This is the first attempt to apply the IPMC material in the field of precision positioning platforms.

The remainder of this article is organized as follows. The required materials, fabrication process, and experimental setup of the helical IPMC actuator are presented in Section 2. Then, its actuation behaviors and characteristics, including axial displacement, axial force, electric current, and cyclic voltammetry (CV) curves, are evaluated in Section 3. Moreover, the actuator is meshed, modeled, and analyzed in Section 4. The prototype of a 3-DOF micro-parallel platform with three helical IPMC actuators is shown in Section 4. Finally, conclusions of the present research are drawn in Section 5.

## 2. Materials and Methods

### 2.1. Materials

A commercial membrane Nafion-117 with a thickness of 0.18 mm was purchased from DuPont Company (Wilmington, DE, USA).  $[\text{Pt}(\text{NH}_3)_4]\text{Cl}_2$ ,  $\text{NaBH}_4$ ,  $\text{NH}_2\text{NH}_2 \cdot 1.5\text{H}_2\text{O}$ , and  $\text{NH}_2\text{OH} \cdot \text{HCl}$  were provided by Sigma Aldrich (St. Louis, MO, USA).  $\text{NaOH}$ ,  $\text{LiCl}$ , and  $\text{LiOH}$  were obtained from Nanjing Chemical Reagent Co., Ltd. (Nanjing, China).

### 2.2. Fabrication

There are two main methods to fabricate a helical IPMC: chemical and physical. As for the former, an IPMC with a three-dimensional shape is obtained by melt-processing the perfluorinated ionic polymer in the form of raw resin; then, it must be chemically treated (hydrolyzed) to become ionic [29]. Obviously, this method is somewhat complicated. In contrast, the latter method is relatively simple, which is to fix the helical shape by thermal treatment [28] or coating at room temperature [30]. In this paper, the physical method was employed. The process involved is shown in Figure 1a, detailed as follows:

1. Cut the commercial membrane Nafion-117 into a strip;
2. Deposit platinum nanoparticles on both surfaces of the Nafion membrane by electrodeless plating to obtain an IPMC strip [31];
3. Coil the IPMC strip in a prepared mold with helix grooves, and put a Teflon tube outside the mold to prevent the IPMC strip from expanding outward and releasing from the mold;
4. Immerse the mold in deionized water at  $90^\circ\text{C}$  for 5 h;
5. Remove the helical IPMC from the mold.

The fabricated specimen is shown in Figure 1b, and its structural parameters are listed in Table 1.

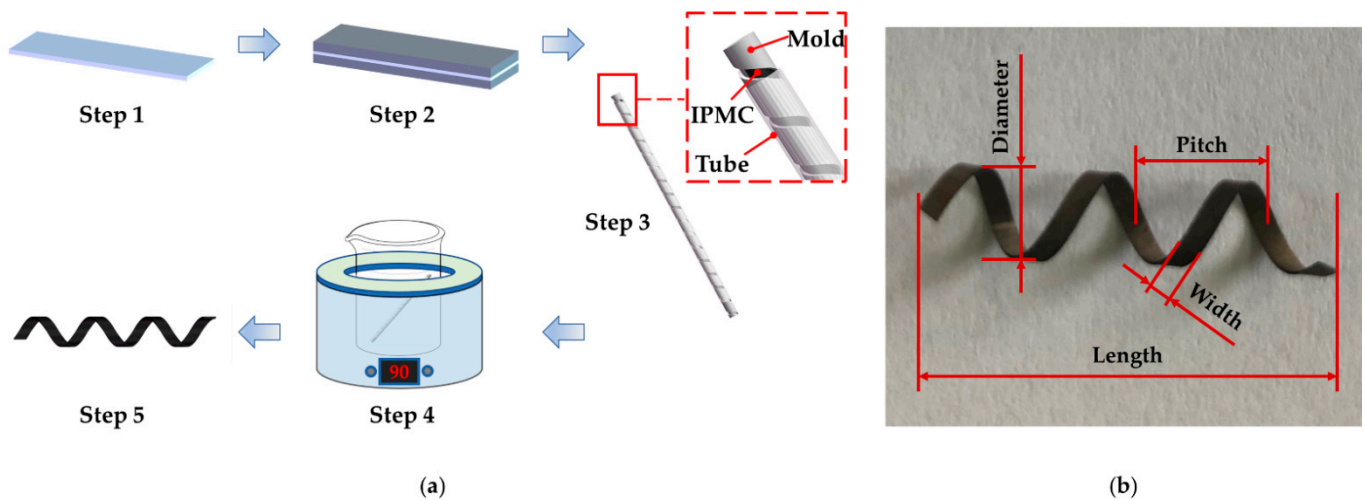


Figure 1. (a) Fabrication process of the helical IPMC; (b) a photograph of the specimen.

Table 1. Parameters of the helical IPMC specimen.

Diameter (mm)	Pitch (mm)	Length (mm)	Width (mm)	Weight (mg)
5.00	6.47	20.09	1.49	20.2

### 2.3. Experimental Setup

In the electromechanical test, the experimental setup (shown in Figure 2a) was composed of a signal generator, a high-speed camera, a load cell, a current sensor, a clamping device, and an industrial computer. A signal generator (JDS6600, JUNTEK, Hangzhou, China) produced various electrical signals. The motion behaviors of the helical IPMC actuator were captured and recorded by a high-speed camera (i-SPEED 3, Olympus, Tokyo, Japan), and then the image information was processed to obtain the axial displacement data. The force of the helical IPMC actuator expanding along the axial direction (hereinafter referred to as axial force) was measured by a load cell (20 g, AVIC ZEMIC, Xi'an, China). Before the measurement, the helical IPMC actuator contracted to the shortest state by an electric field, and then its end point was in contact with the surface of the load cell. Afterward, a reverse voltage was applied to make it elongate, so that the axial force data obtained in this experiment were continuous. A current sensor (self-made current acquisition system embedded with STM32F405RGT6 chip) was employed to detect and display the corresponding electric current. A clamping device was used to fix the specimen and adjust its height. Last but not least, an industrial computer controlled the whole system. This test was conducted in air at room temperature.

In the electrochemical test, a three-electrode system was used to evaluate the electrochemical characteristics of the actuator, as shown in Figure 2b. Platinum electrodes on both sides of the IPMC served as the working electrode and counter electrode, an Ag/AgCl electrode served as the reference electrode, and 1 M of hydrochloric acid solution served as the electrolyte. The CV curves of the helical IPMC actuator were obtained by an electrochemical workstation (CHI604E, Shanghai Chenhua Instrument Co., Ltd., Shanghai, China). The scanning rates were set to 100 mV, 200 mV, 500 mV, 1000 mV, and 2000 mV, and the voltage range was set to  $-0.5$  V to  $0.5$  V [22].

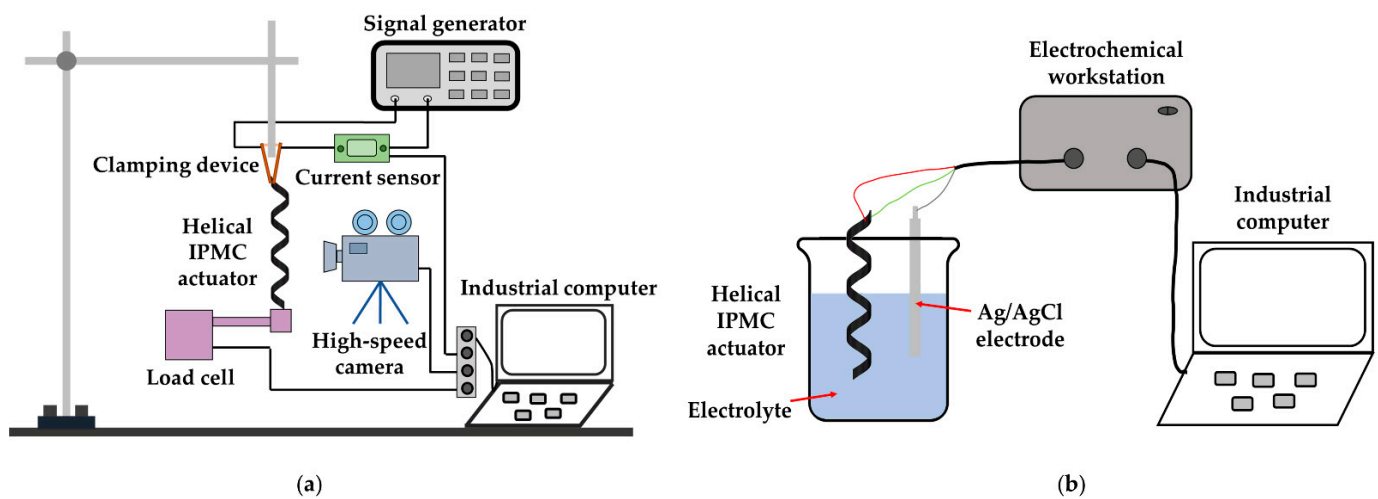


**Figure 2.** Experimental setup for the helical IPMC actuator: (a) electromechanical test; (b) electrochemical test.

### 3. Results and Discussions

#### 3.1. Actuation Behaviors

A high-speed camera was used to observe the motion behaviors of the helical IPMC actuator from the frontal direction. The actuated signal was a sinusoidal wave of 3.5 V and 0.1 Hz. The captured images are shown in Figure 3 and Video S1, and the time interval of each image is 1 s.

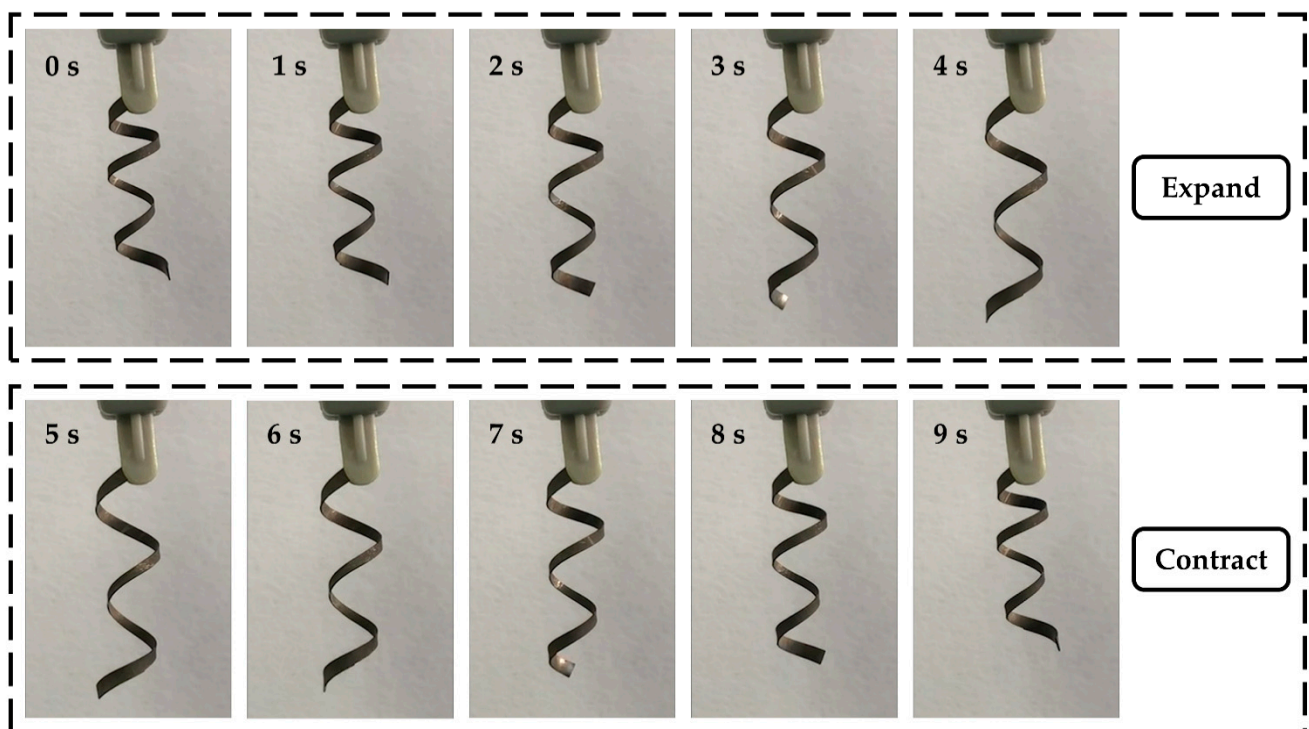


**Figure 3.** Three-dimensional motion of the helical IPMC actuator in a sinusoidal period.

From the figure, it can be seen that the helical IPMC actuator is able to generate complicated three-dimensional motion under the stimulation of the electric field, which can be decomposed into three branches: radial movement, axial movement, and torsional movement. This phenomenon is attributed to the electro-active properties of the IPMC and the particularity of the actuator's shape. The actuation principle of IPMC is shown

in Figure 4. After an electric field is applied between the two deposited electrodes, the hydrated cations inside the polymer membrane rapidly migrate to the cathode. Due to the uneven distribution of water molecules, the IPMC bends toward the anode side. This internal ion-water movement like electrophoresis produces effective strains for actuation [32]. Considering our actuator, if there is no electric field, it is in a natural state. When a positive voltage is applied to the outer surface of the actuator while a negative voltage is applied to the inner surface, the water molecules carried by cations inside the polymer membrane will migrate to the inner surface side, resulting in increases in stress and strain here. On this account, the helical IPMC expands as the number of turns decreases and the pitch increases, which causes the actuator to elongate along the axial direction. In contrast, when an opposite voltage is applied, the stress and strain of the outer surface side will increase and the actuator will tend to contract tightly, leading to its axial shortening. The behaviors of the helical IPMC actuator are abstracted and presented in Figure 5.

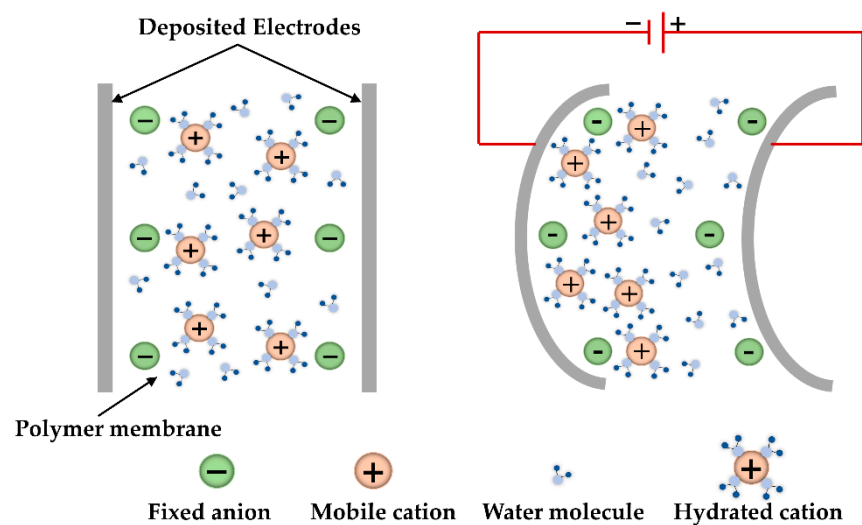


**Figure 4.** Actuation principle of a typical strip-shaped IPMC.

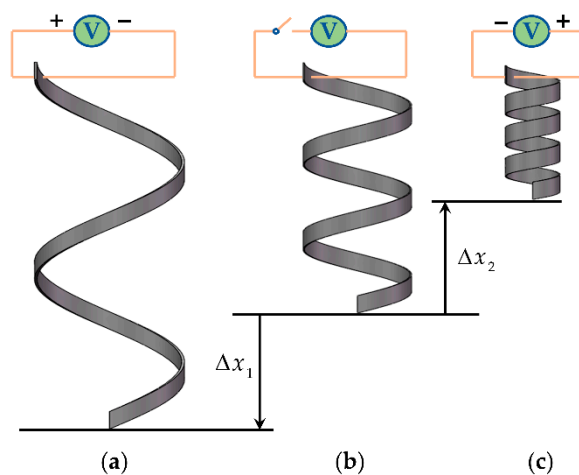


**Figure 5.** Schematic diagram of the helical IPMC actuator: (a) elongated state; (b) natural state; (c) shortened state.

### 3.2. Displacement Characteristics

The axial displacement intuitively demonstrates the linear actuation performance of the helical IPMC actuator. Figure 6 shows the axial displacement responses of the helical IPMC actuator driven by three different electrical signals (see Appendix A for the detailed repeatability test). It is worth noting that the excitation frequencies of the sinusoidal and

square wave signals are both 0.1 Hz. As shown in the figure, as the voltage amplitude increases, the axial displacement of the helical IPMC actuator increases correspondingly. This is because the higher voltage drives more hydrated cations to migrate to the cathode, which greatly increases the stress and strain on the inner or outer surface of the helical IPMC. Macroscopically, the actuator has greater deformation, which means the value of  $\Delta x_1 + \Delta x_2$  shown in Figure 5 increases.

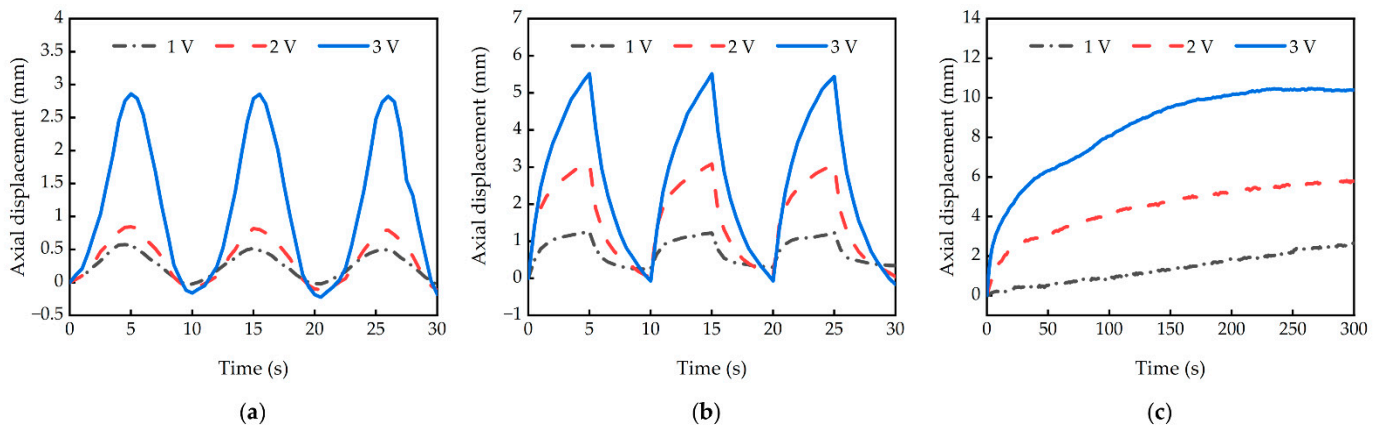


**Figure 6.** Axial displacements of the helical IPMC actuator under different signals with different amplitudes: (a) sinusoidal signal; (b) square wave signal; (c) DC signal.

When a sinusoidal signal is input, as shown in Figure 6a, the axial displacement curve of the helical IPMC actuator exhibits a sinusoidal trend as well. At voltage amplitudes of 1 V, 2 V, and 3 V, the maximum axial displacements are 0.57 mm, 0.84 mm, and 2.86 mm, respectively. When a square wave signal is input, as shown in Figure 6b, once the actuator reaches the peak displacement, it rapidly reverses its motion direction; thus, sharp points appear on the curve. At 1 V, 2 V, and 3 V, the maximum axial displacements are 1.25 mm, 3.13 mm, and 5.52 mm, respectively, which are 119%, 272%, and 93% larger than those driven by the sinusoidal signal. During the 30 s test period, the axial displacement response of the helical IPMC actuator has good repeatability under either sinusoidal signal or square wave signal. In stark contrast, when a DC signal is input, the axial displacement of the actuator rises slowly and has no periodicity, as shown in Figure 6c. At 1 V, 2 V, and 3 V, the actuator reaches the maximum axial displacements of 2.66 mm, 5.82 mm, and 10.47 mm, respectively, which are increased by 113%, 86%, and 90% compared with those driven by square wave signal. As the moisture loss (evaporation and electrolysis) inside the polymer membrane accelerates under the DC signal, it takes a longer time to reach the maximum axial displacement. If the working time is not taken into account, the helical IPMC actuator driven by the DC signal presents the best axial motion.

In addition to the waveform and amplitude of the input signal, the frequency also has a great influence on the axial displacement of the helical IPMC actuator. The related curves are plotted in Figure 7, in which the applied voltage is 3 V. The presented results indicate that the axial displacement of the actuator decreases with the excitation frequency. This phenomenon is due to the fact that the time for the movement of the hydrated cations inside the polymer membrane toward the cathode is not sufficient [33]. At 0.25 Hz, 0.5 Hz, and 1 Hz, the maximum axial displacements of the actuator driven by the sinusoidal signal are measured to be 1.68 mm, 1.26 mm, and 0.77 mm, respectively. Under the square wave signal, the maximum displacements are measured to be 3.84 mm, 2.17 mm, and 1.26 mm, respectively. The results show that at any frequency, the maximum axial displacement of the helical IPMC actuator driven by a square wave signal is always greater than that driven by a sinusoidal signal. More importantly, because of the unique relationship between input and output, the axial displacement of the helical IPMC actuator can be accurately controlled by input signals.

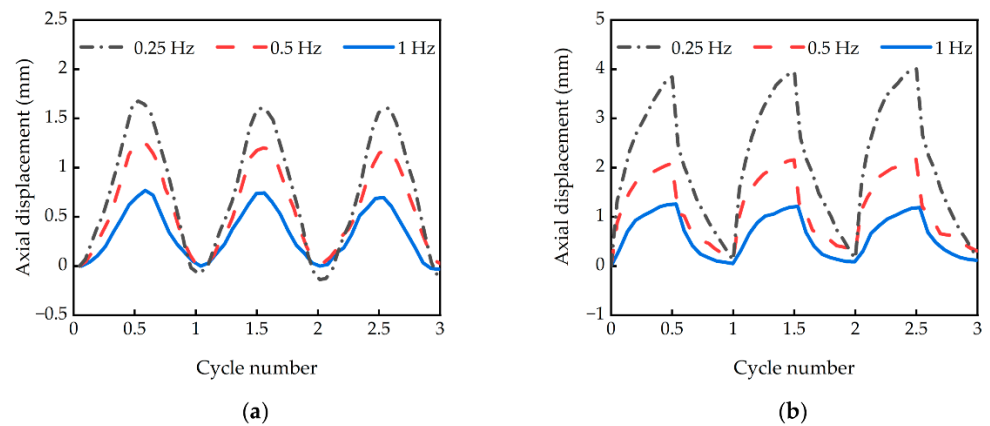


**Figure 7.** Axial displacements of the helical IPMC actuator under different signals with different frequencies: (a) sinusoidal signal; (b) square wave signal.

### 3.3. Force Characteristics

The axial force is another important parameter to evaluate the actuation performance of the helical IPMC actuator. Figure 8 illustrates the effect of voltage amplitude on the axial force of the actuator, and the frequency of the sinusoidal signal and square wave signal shown in the figure is 0.1 Hz.

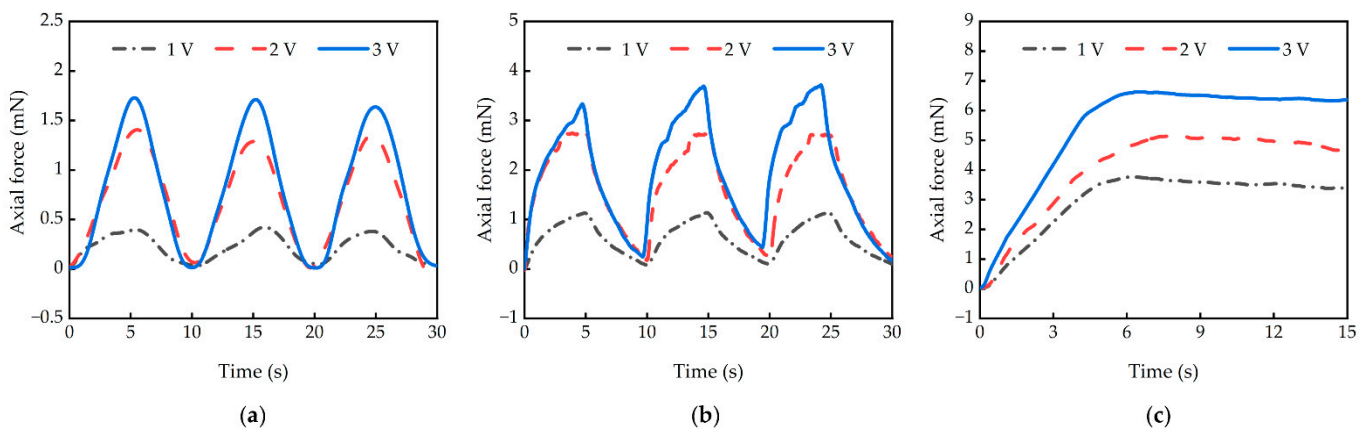


**Figure 8.** Axial forces of the helical IPMC actuator under different signals with different amplitudes: (a) sinusoidal signal; (b) square wave signal; (c) DC signal.

The axial force characteristics of the helical IPMC actuator are similar to the axial displacement characteristics. Likewise, it can be concluded that as the voltage amplitude increases, the axial force increases correspondingly. In addition, the axial forces of the actuator under the sinusoidal signal and square wave signal are both periodic, while the force under the DC signal is in a single direction, which is instructive for different applications. Under a DC signal of 3 V, the actuator reaches its maximum axial force of 6.63 mN at 6.57 s.

Under an AC signal of 3 V, the axial force responses of the actuator at different frequencies are shown in Figure 9. The results indicate that the axial force decreases with the frequency. Furthermore, the helical IPMC actuator driven by a square wave signal produces a greater axial force when experimental conditions are identical.

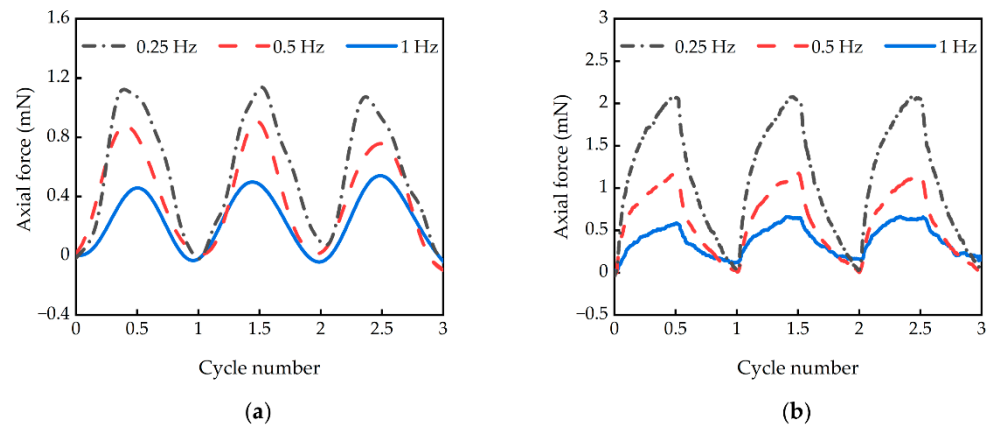


**Figure 9.** Axial forces of the helical IPMC actuator under different signals with different frequencies: (a) sinusoidal signal; (b) square wave signal.

### 3.4. Electric Current Characteristics

The electric current characteristics of the helical IPMC actuator can also reflect its actuation performance to a certain extent. The electric current of the IPMC is believed to originate from the migration of hydrated cations between two electrodes [34]. The more hydrated cations migrate, the greater the electric current. It can be seen from Figures 10 and 11 that the current increases with the increase in voltage and decrease in frequency, which is the same as the above-mentioned conclusions. However, the trend of the electric current curve is completely different from those of axial displacement and force curves. The electric current of the helical IPMC actuator under the sinusoidal signal does not present a perfect sinusoidal curve, which is related to the nonlinear characteristics of the material. When the input signal is a square wave or DC, the current reaches its peak in an instant, and then drops to a stable state within a few seconds. Under a DC signal of 3 V, the maximum electric current is 45.5 mA.

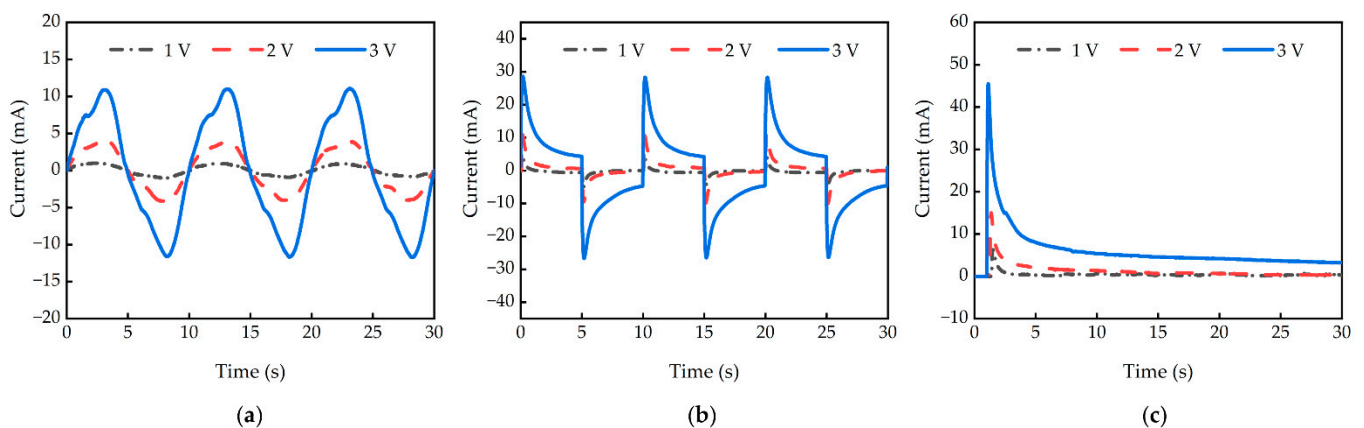


**Figure 10.** Electric currents of the helical IPMC actuator under different signals with different amplitudes: (a) sinusoidal signal; (b) square wave signal; (c) DC signal.

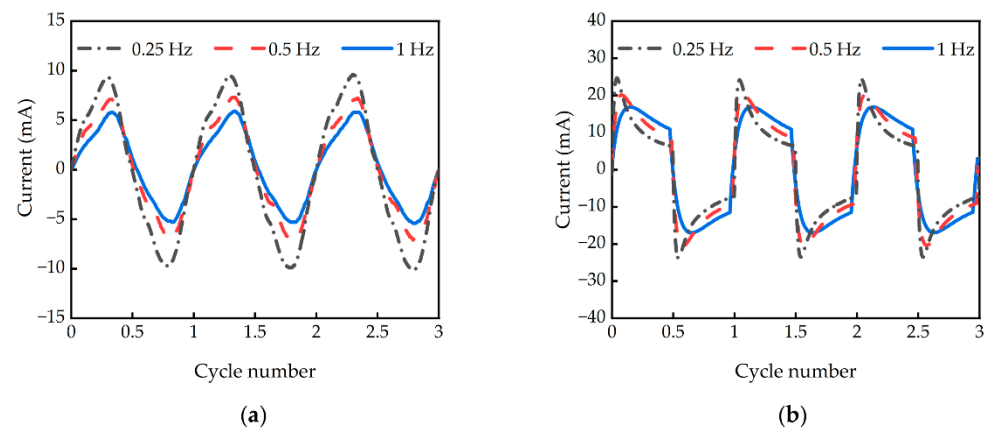


**Figure 11.** Electric currents of the helical IPMC actuator under different signals with different frequencies: (a) sinusoidal signal; (b) square wave signal.

### 3.5. Electrochemical Characteristics

In order to probe into the electrochemical characteristics of the helical IPMC actuator, its voltage/current response was measured by cyclic voltammetry. The experimental results are shown in Figure 12a. In the measured reversible CV curves, there are no obvious redox peaks during a charge–discharge cycle, and the curve shape is approximately rectangular. This means that under given conditions, the fabricated helical IPMC actuator is chemically stable and can be used as an ideal double-layer capacitor.

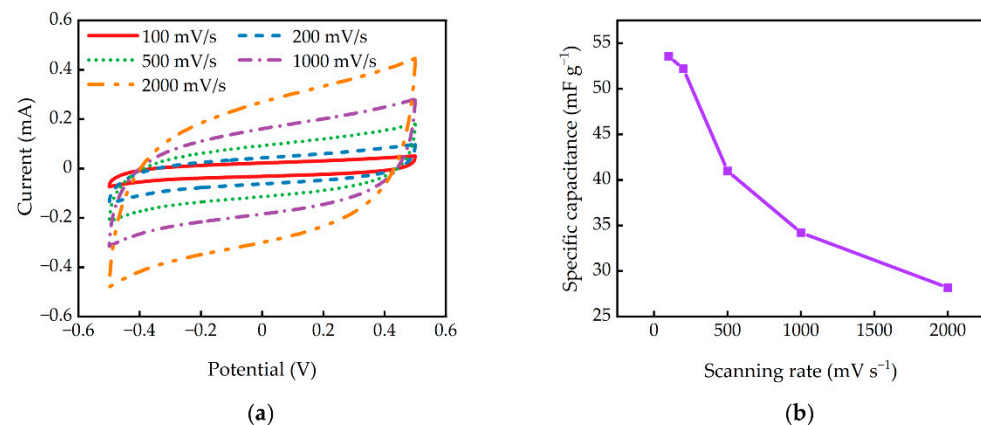


**Figure 12.** Electrochemical test results at different scanning rates: (a) CV; (b) gravimetric specific capacitance.

The gravimetric specific capacitance  $C_g$  of the helical IPMC actuator can be evaluated by the following formula:

$$C_g = \frac{2I_p}{V_s m}, \quad (1)$$

where  $I_p$  is the peak-to-peak value of the current when the voltage is 0 V,  $V_s$  is the scanning rate of the voltage ( $\text{V}\cdot\text{s}^{-1}$ ) [35], and  $m$  is the weight of the helical IPMC actuator. The calculation results are presented in Figure 12b. As the scanning rate increases, the gravimetric specific capacitance decreases. When the scanning rate is  $100 \text{ mV}\cdot\text{s}^{-1}$ , the calculated gravimetric specific capacitance is  $53.56 \text{ mF}\cdot\text{g}^{-1}$ , which is approximately 2.8 times that of the value for the IPMC reported by Ma et al. [22]. Large capacitance may be conducive to forming an excellent electric double layer at the electrode interface [22], thereby facilitating ion diffusion and charge accumulation.

#### 4. Modeling and Simulation

It is essential to model and simulate the helical IPMC actuator to enhance the predictability of its actuation behaviors before it is used in practical application. Similar to other IPMC models [36–39], we regard the helical IPMC as a cantilever beam. Three physical phenomena are mainly considered: (i) electrical signals applied externally; (ii) cation migration inside the polymer; (iii) macroscopic deformation caused by the stress difference between the inner and outer surfaces. COMSOL Multiphysics 5.6 (a cross-platform finite element analysis, solver, and multiphysics simulation software) is utilized for geometry and material description, meshing, and calculation, involving multi-field coupling among Electrostatics, Transport of Diluted Species, and Solid Mechanics modules.

##### 4.1. Mass Transfer Model

The mass transfer model of the IPMC was used to describe the transport process of cations and water molecules inside the polymer membrane under the action of electric field or force, which includes the friction model [40], irreversible thermodynamic model [41], and Nernst–Planck model [42]. Among them, the Nernst–Planck model is the most widely accepted at present, and its general form is [43–45]:

$$\frac{\partial C}{\partial t} = -\nabla \cdot J, \quad (2)$$

$$J = -\left(D\nabla C - uC - \frac{zeDEC}{K_B T}\right), \quad (3)$$

$$E = -\nabla\Phi - \frac{\partial \mathbf{B}}{\partial t}, \quad (4)$$

where  $J$ ,  $D$ ,  $C$ , and  $z$  are the flux, diffusion coefficient, concentration, and charge number of mobile ions (here, hydrated cations), respectively,  $t$  is the time,  $e$  is the elementary charge,  $K_B$  is the Boltzmann constant,  $T$  is the absolute temperature,  $u$  is the fluid velocity,  $E$  is the electric field intensity,  $\Phi$  is the electric potential, and  $\mathbf{B}$  is the magnetic field vector. The Nafion membrane is regarded as a static system and IPMC usually works under a static magnetic field; thus,  $u = 0$  and  $\partial \mathbf{B} / \partial t = 0$ .

According to the Nernst–Planck equation, the diffusion coefficient of the mobile ions  $D$  can be correlated with their mobility  $\mu$  [46]:

$$D = \mu RT, \quad (5)$$

where  $R$  is the gas constant, given by:

$$R = K_B N_A = \frac{K_B F}{e}, \quad (6)$$

in which  $N_A$  is the Avogadro constant and  $F$  is the Faraday constant. Thus, the final form of the Nernst–Planck equation is:

$$\frac{\partial C}{\partial t} = \nabla \cdot (D\nabla C + \mu z F C \nabla \Phi). \quad (7)$$

Furthermore, for coupling the ion transport field with the electrostatic field, it is also required to consider the Poisson equation [47]:

$$\nabla^2 \Phi = -\frac{\rho}{\varepsilon}, \quad (8)$$

where  $\varepsilon$  stands for the absolute dielectric permittivity and  $\rho$  stands for the space charge density, which is defined as:

$$\rho = F(C - C_0), \quad (9)$$

where  $C_0$  represents the concentration of anions, which is a constant as the anions are immovable inside the Nafion membrane.

#### 4.2. Hygroscopic Swelling Model

In previous experiments, it was found that the volume of the Nafion membrane would increase due to the change in internal stress after contacting with water or other liquids. We call this phenomenon the hygroscopic swelling property of the Nafion membrane. Assuming that the volume change  $\Delta V$  has a linear relationship with the water absorption quality  $\Delta m$ ,

$$\Delta V = \beta_h \Delta m, \quad (10)$$

where  $\beta_h$  is defined as the hygroscopic swelling coefficient. The difference between the volume  $V$  after swelling and the volume  $V_0$  before swelling can be calculated as:

$$V - V_0 = lwh - l_0w_0h_0, \quad (11)$$

in which  $l_0$  and  $l$ ,  $w_0$  and  $w$ , and  $h_0$  and  $h$  are the length, width, and thickness before and after swelling, respectively. Assuming that the Nafion membrane is an ideal elastomer and its linear strain is  $\alpha$ , then:

$$\lim_{l_0 \rightarrow 0} \frac{l}{l_0} = \lim_{w_0 \rightarrow 0} \frac{w}{w_0} = \lim_{h_0 \rightarrow 0} \frac{h}{h_0} = \alpha + 1. \quad (12)$$

Hence,

$$\lim_{V_0 \rightarrow 0} \frac{\Delta V}{V_0} = (\alpha + 1)^3 - 1. \quad (13)$$

The water absorption quality  $\Delta m$  can be obtained by the following equation:

$$\Delta m = MVC - MV_0C_0 \approx MV_0(C - C_0), \quad (14)$$

where  $M$  is the molar mass of the cations. Finally, the relationship between the linear strain of the Nafion membrane  $\alpha$  and the concentration of the mobile ions  $C$  can be derived as follows:

$$\alpha = \sqrt[3]{\beta_h M(C - C_0) + 1} - 1. \quad (15)$$

#### 4.3. Boundary and Initial Conditions

In the electrostatic field, we require that the surface potential of the helical IPMC actuator changes periodically with time:

$$\Phi = A \sin(2\pi ft). \quad (16)$$

In the ion transport field, the solute leakage from electrode surfaces is ignored, that is, the ion flux of each surface is zero. When  $t = 0$ , the concentration of the mobile ions inside the Nafion membrane is set to  $C_0$ .

In the solid mechanics field, the helical IPMC is regarded as a cantilever beam. One end is fixed and the displacement  $u(x, y, z) = 0$ , while the other end is free to deform without constraint.

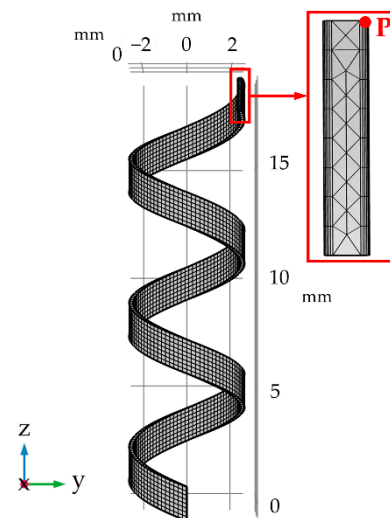
#### 4.4. Model Parameters and Meshing

The physical parameters contained in the above equations, as well as the geometric and material parameters required for model establishment, are summarized in Table 2. Some of them have been obtained from our previous experiments, and some are from references [39,48].

**Table 2.** Related parameters of the model.

Variable/Constant	Value and Unit
Faraday constant, $F$	96,485.332 C/mol
Mobility, $\mu$	$2.9 \times 10^{-15}$ s·mol/kg
Diffusion coefficient, $D$	$1 \times 10^{-10}$ m <sup>2</sup> /s
Charge number, $z$	1
Permittivity of Nafion membrane, $\epsilon$	$2.8 \times 10^{-3}$ F/m
Concentration of anions, $C_0$	1000 mol·m <sup>3</sup>
Absolute temperature, $T$	293 K
Young's modulus of IPMC, $E_{IPMC}$	0.5 GPa
Poisson's ratio of IPMC, $\nu_{IPMC}$	0.487
Density of IPMC, $\rho_{IPMC}$	2600 kg/m <sup>3</sup>
Molar mass of cations, $M$	0.0789 kg/mol
Hygroscopic swelling coefficient, $\beta_h$	$0.32 \times 10^{-3}$ m <sup>3</sup> /kg
Amplitude of applied voltage, $A$	1 V, 2 V, 3 V
Frequency of applied voltage, $f$	0.25 Hz, 0.5 Hz, 1 Hz

In COMSOL Multiphysics software, the partial differential equation (PDE) module was adopted to simulate the helical IPMC actuator. A free triangular mesh was created for the geometric model, and one was refined near the electrode surfaces to enhance the calculation accuracy. Solution convergence was found to be highly affected by the size of the mesh. In our model, the entire mesh contained 26,656 domain elements, 9268 boundary elements, and 1028 edge elements, with an average quality of 0.7026, as shown in Figure 13.

**Figure 13.** Mesh distribution of the helical IPMC actuator.

#### 4.5. Data Analysis and Model Verification

In this work, for the sake of simplicity, we only considered the sinusoidal wave as the input signal, and employed a transient solver. For the axial displacement of the end point P (shown in Figure 13), Figures 14 and 15 present the comparison between the experimental data (see Section 3.2) and the simulated data. It can be seen that the simulation curve maintains good consistency with the experiment curve under the condition of voltage transformation or frequency conversion. Errors may be caused by the simplified factors in the modeling process, which need to be further optimized in the future.

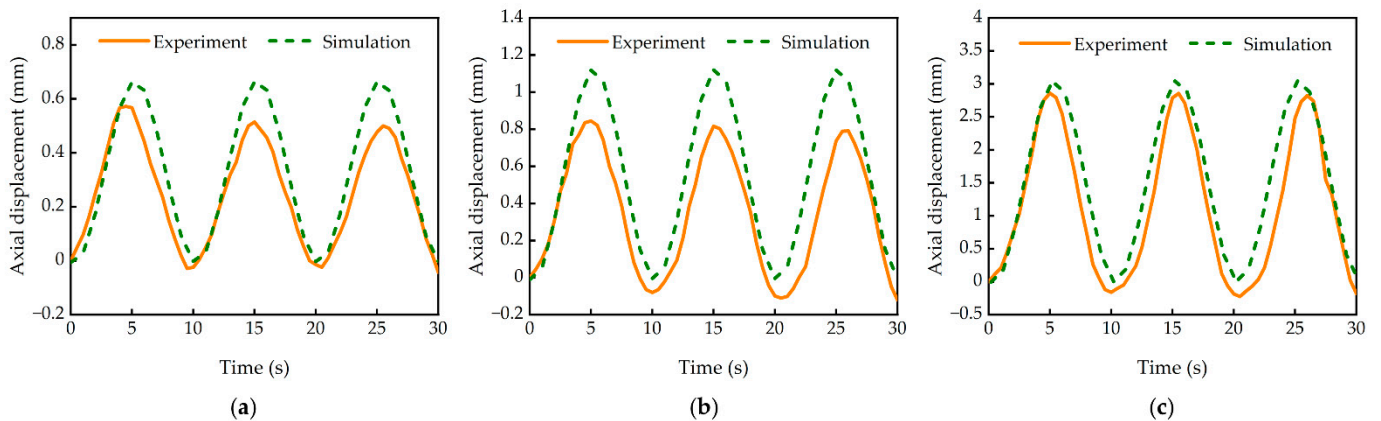


**Figure 14.** Experimental and simulated data of axial displacement of the helical IPMC actuator under sinusoidal signals with different amplitudes: (a) 1 V, 0.1 Hz; (b) 2 V, 0.1 Hz; (c) 3 V, 0.1 Hz.

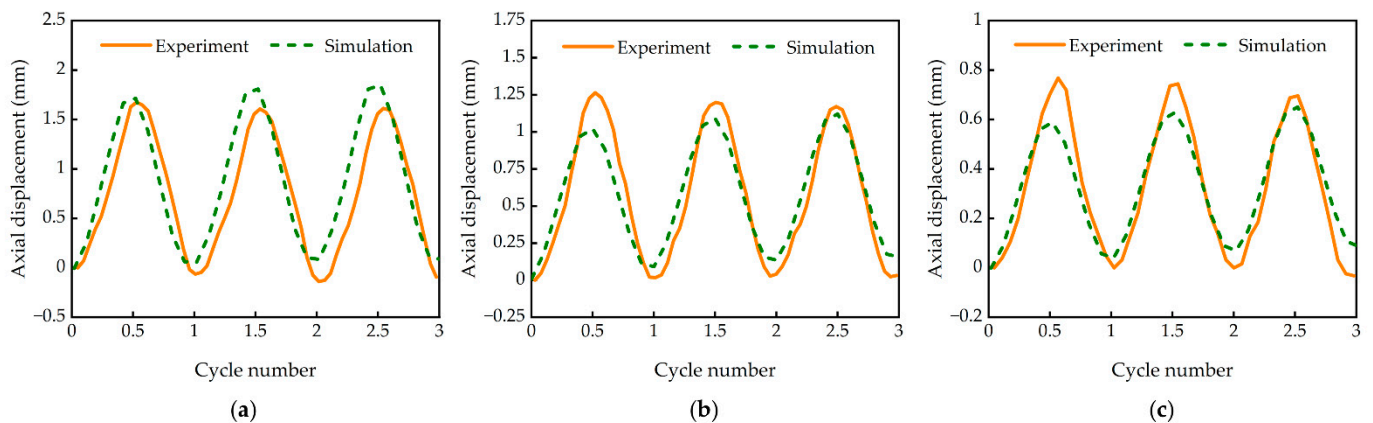


**Figure 15.** Experimental and simulated data of axial displacement of the helical IPMC actuator under sinusoidal signals with different frequencies: (a) 3 V, 0.25 Hz; (b) 3 V, 0.5 Hz; (c) 3 V, 1 Hz.

Figures 16 and 17 show the concentration of the mobile ions and the von Mises stress in a period, respectively. At 0–4 s, the hydrated cations inside the Nafion membrane are densely distributed on the outer surface side, and the stress here is obviously greater than that near the inner surface, which makes the actuator tend to contract. At 5–9 s, the dense area of the hydrated cations is transferred to the inner surface side, where the stress is greater than that near the outer surface, giving the actuator a tendency to expand. This simulation result verifies the actuation principle of the helical IPMC actuator.

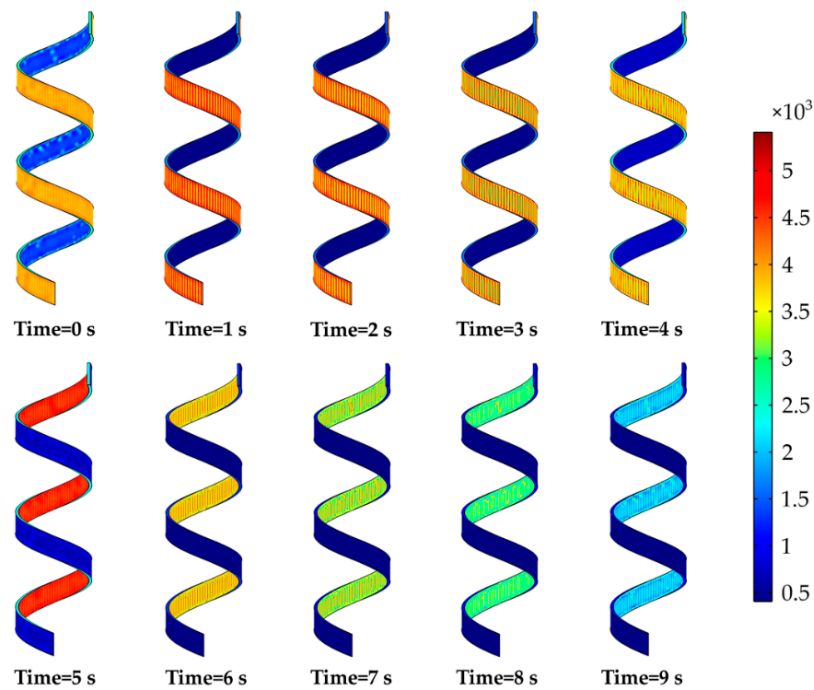


Figure 16. Concentration distribution of the mobile ions.

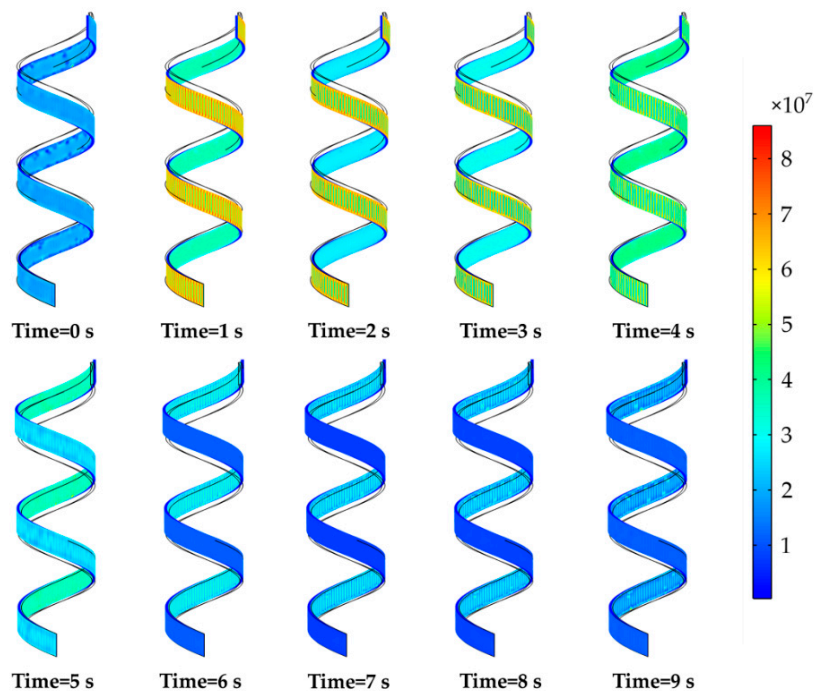
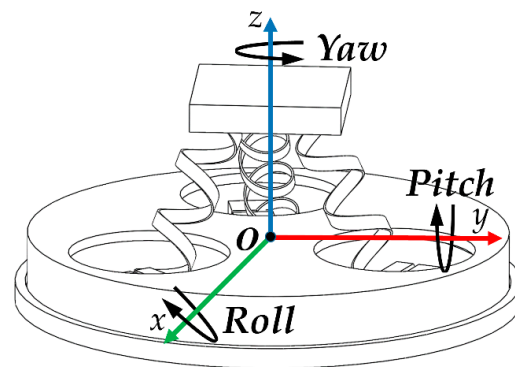


Figure 17. Cloud map of the von Mises stress.

### 5. Application to a 3-DOF Micro-Parallel Platform

Considering the unique performance of the helical IPMC actuator, a novel type of flexible 3-DOF micro-parallel platform was developed (shown in Figure 18). The device comprised a base part, a driving part, and a movable platform. The base part was made of resin material by 3D printing, which was responsible for clamping the actuators and sending signals to them. The driving part consisted of three helical IPMC actuators with the same structural parameters of diameter, pitch, width, and length. Finally, the movable platform was a light carton with a weight of 40 mg.



**Figure 18.** 3D model of the 3-DOF micro-parallel platform.

The deformation of the three helical IPMC actuators generated by electrical signals enables the movable platform to realize a 3-DOF coupling movement of pitch, roll, and yaw (Figure 19 and Video S2). The device possesses three linear-motion driving units, which are consistent with the DOF of the movable platform; thus, there is no actuation redundancy in this case. When DC signals in range of  $-3\text{ V}$  to  $3\text{ V}$  are input, the pitch angle that the movable platform can reach is about  $30^\circ$ , the roll angle is about  $30^\circ$ , and the yaw angle is about  $45^\circ$ . Compared with conventional 3-DOF platforms, the newly designed micro-parallel platform has the advantages of simple structure, good compliance, low power consumption, and easy miniaturization, which can meet the requirements of small size, millimeter-level stroke, and high stability.

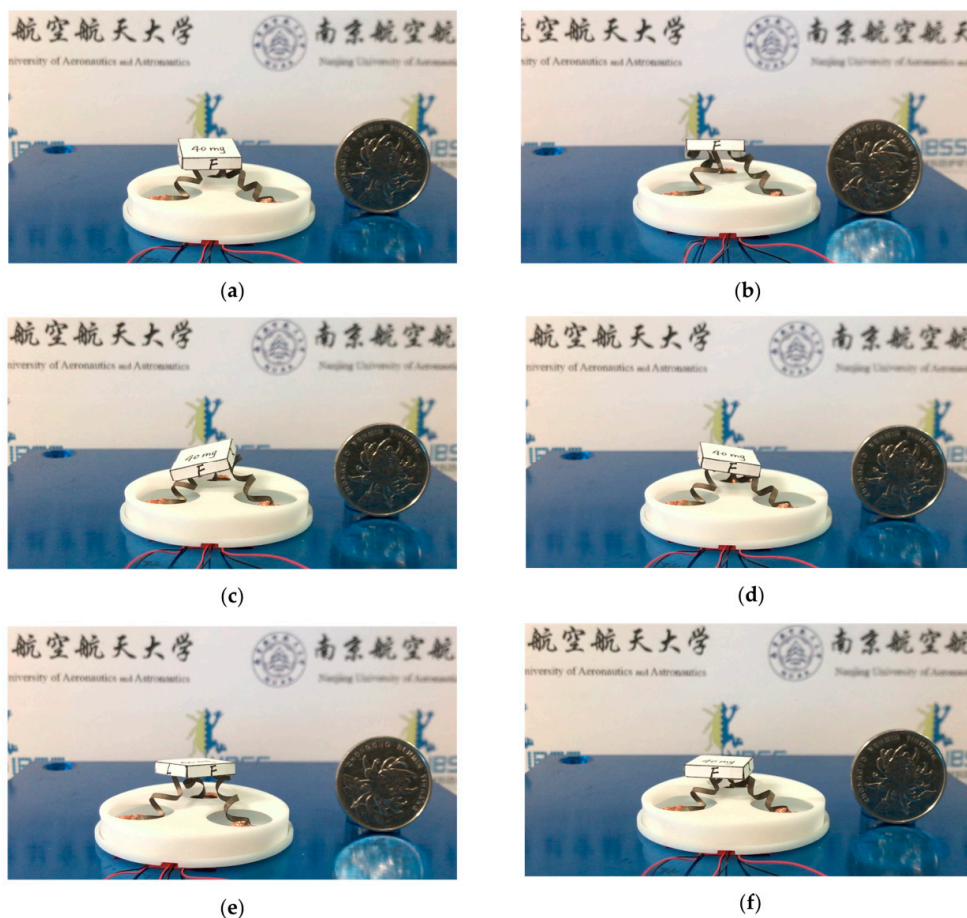


**Figure 19.** Coupling movement of the 3-DOF micro-parallel platform based on helical IPMC actuator: (a,b) pitch; (c,d) roll; (e,f) yaw.

## 6. Conclusions

In this paper, a helical IPMC was fabricated in a water bath by using a mold with helix grooves. Due to the electroactivity of the material and the particularity of the designed shape, the helical IPMC can produce complicated three-dimensional motion. We paid more attention to its axial movement and tried to apply it in practice, which differentiates from others' work. For evaluating its actuation performance, the axial displacement, axial force, and electric current were tested and analyzed. It was found that with the increase in the voltage amplitude and the decrease in the excitation frequency, the actuator tended to work better (larger displacement and higher axial force). In addition, the electrochemical test results showed that the actuator had good chemical stability. To enhance the predictability of the actuation behaviors, we coupled several physical fields and established a model. The simulation results were basically consistent with the experimental results. In the last part of this work, a 3-DOF micro-parallel platform with three helical IPMC actuators as driving components was designed and manufactured, and it could generate a coupling movement of pitch, roll, and yaw under the electric field. By controlling the input signal, precise positioning could be realized. This research promotes the multi-scale development of smart materials and the wide application of multi-DOF precision platforms. Future research will concentrate on the performance improvement of the actuator, accuracy optimization of the model, and cooperative control of the 3-DOF platform.

**Supplementary Materials:** The following are available online at <https://www.mdpi.com/article/10.3390/act10100248/s1>, Video S1: Three-dimensional motion of the helical IPMC actuator, Video S2: Coupling movement of the 3-DOF micro-parallel platform.

**Author Contributions:** Conceptualization, Y.W. and M.Y.; methodology, Y.W. and Q.H.; software, D.V.; formal analysis, Y.W. and G.Y.; investigation, Y.W., G.Y. and X.X.; resources, P.L.; writing—original draft preparation, Y.W., X.X. and P.L.; writing—review and editing, Q.H. and D.V.; supervision, Q.H.; project administration, M.Y. and Q.H.; funding acquisition, M.Y. and Q.H. All authors have read and agreed to the published version of the manuscript.

**Funding:** This research was funded by the National Natural Science Foundation of China, grant numbers 51605220 and U1637101, the Natural Science Foundation of Jiangsu Province of China, grant number BK20160793, and the Fundamental Research Funds for the Central Universities, grant number NS2020029.

**Institutional Review Board Statement:** Not applicable.

**Informed Consent Statement:** Not applicable.

**Data Availability Statement:** The data presented in this study are available on request from the corresponding author.

**Conflicts of Interest:** The authors declare no conflict of interest.

## Appendix A

To investigate the performance stability of the helical IPMC actuator, a repeatability test was carried out. Under sinusoidal and square wave signals of 3 V, 0.1 Hz, the axial displacements in 100 cycles were measured, respectively. The experimental results are shown in Figure A1. It can be found that when a sinusoidal signal is input, there is no significant reduction in axial displacement during the test period, indicating that the actuator has stable actuation performance. However, when a square wave signal is input, the axial displacement begins to decrease after about 10 cycles and declines by 41% after 50 cycles. The reason for this phenomenon may be that the large deformation driven by the square wave signal leads to an acceleration of the water evaporation and electrolysis inside the polymer membrane.

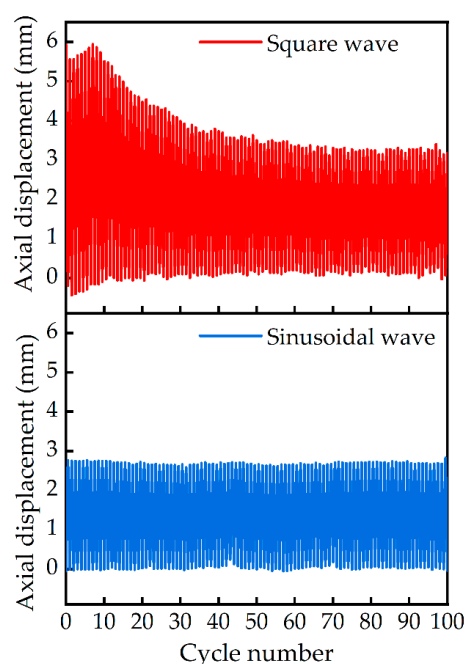


**Figure A1.** The axial displacements of the helical IPMC actuator within 100 cycles under the input signal of 3 V, 0.1 Hz.

## References

1. Yan, Y.; Hu, Z.; Zhao, X.; Sun, T.; Dong, S.; Li, X. Top-down nanomechanical machining of three-dimensional nanostructures by atomic force microscopy. *Small* **2010**, *6*, 724–728. [\[CrossRef\]](#)
2. Holub, O.; Spiller, M.; Hurak, Z. Stick-slip based micropositioning stage for transmission electron microscope. In Proceedings of the 9th IEEE International Workshop on Advanced Motion Control, Istanbul, Turkey, 27–29 March 2006; pp. 484–487. [\[CrossRef\]](#)
3. Hesselbach, J.; Wrege, J.; Raatz, A.; Becker, O. Aspects on design of high precision parallel robots. *Assem. Autom.* **2004**, *24*, 49–57. [\[CrossRef\]](#)
4. Adibnazari, I.; Nagel, W.S.; Leang, K.K. A 3D-printed 3-DOF tripod robotic platform for unconstrained and omnidirectional sample positioning. *Int. J. Intell. Robot.* **2018**, *2*, 425–435. [\[CrossRef\]](#)
5. Li, Y.; Xu, Q. Design and analysis of a totally decoupled flexure-based XY parallel micromanipulator. *IEEE Trans. Robot.* **2009**, *25*, 645–657. [\[CrossRef\]](#)
6. Li, Y.; Xu, Q. Modeling and performance evaluation of a flexure-based XY parallel micromanipulator. *Mech. Mach. Theory* **2009**, *44*, 2127–2152. [\[CrossRef\]](#)
7. Kim, H.S.; Cho, Y.M. Design and modeling of a novel 3-DOF precision micro-stage. *Mechatronics* **2009**, *19*, 598–608. [\[CrossRef\]](#)
8. Kim, H.Y.; Ahn, D.H.; Gweon, D.G. Development of a novel 3-degrees of freedom flexure based positioning system. *Rev. Sci. Instrum.* **2012**, *83*, 055114:1–055114:11. [\[CrossRef\]](#) [\[PubMed\]](#)
9. Li, Y.; Huang, J.; Tang, H. A compliant parallel XY micromotion stage with complete kinematic decoupling. *IEEE Trans. Autom. Sci. Eng.* **2012**, *9*, 538–553. [\[CrossRef\]](#)
10. Seo, T.W.; Kim, H.S.; Kang, D.S.; Kim, J. Gain-scheduled robust control of a novel 3-DOF micro parallel positioning platform via a dual stage servo system. *Mechatronics* **2008**, *18*, 495–505. [\[CrossRef\]](#)
11. Tian, Y.; Shirinzadeh, B.; Zhang, D. Design and dynamics of a 3-DOF flexure-based parallel mechanism for micro/nano manipulation. *Microelectron. Eng.* **2010**, *87*, 230–241. [\[CrossRef\]](#)
12. Rodriguez-Fortun, J.M.; Rotella, F.; Alfonso, J.; Carrillo, F.J.; Orus, J. Model-free control of a 3-DOF piezoelectric nanopositioning platform. In Proceedings of the 52nd IEEE conference on decision and control, Florence, Italy, 10–13 December 2013; pp. 342–347.
13. Wang, G.; Wang, Y.; Lv, B.; Ma, R.; Liu, L. Research on a new type of rigid-flexible coupling 3-DOF micro-positioning platform. *Micromachines* **2020**, *11*, 1015. [\[CrossRef\]](#)
14. Chen, K.S.; Trumper, D.L.; Smith, S.T. Design and control for an electromagnetically driven X–Y– $\theta$  stage. *Precis. Eng.-J. Int. Soc. Precis. Eng. Nanotechnol.* **2002**, *26*, 355–369. [\[CrossRef\]](#)
15. Xiao, S.; Li, Y.; Yang, Q. A novel flexure-based 3-DOF micro-parallel manipulator with a gripper for micro/nano manipulation. In Proceedings of the 6th IFAC Symposium on Mechatronic Systems, Hangzhou, China, 10–12 April 2013; pp. 606–611. [\[CrossRef\]](#)
16. Xiao, S.; Li, Y. Optimal design, fabrication, and control of an XY micropositioning stage driven by electromagnetic actuators. *IEEE Trans. Ind. Electron.* **2013**, *60*, 4613–4626. [\[CrossRef\]](#)

17. Nakamura, Y.; Nakayama, M.; Masuda, K.; Tanaka, K.; Yasuda, M.; Fujita, T. Development of active six-degrees-of-freedom microvibration control system using giant magnetostrictive actuators. *Smart Mater. Struct.* **2000**, *9*, 175–185. [[CrossRef](#)]
18. Sun, X.; Yang, B.; Zhao, L.; Sun, X. Optimal design and experimental analyses of a new micro-vibration control payload-platform. *J. Sound Vib.* **2016**, *374*, 43–60. [[CrossRef](#)]
19. Niu, M.; Yang, B.; Yang, Y.; Meng, G. Modelling and parameter design of a 3-DOF compliant platform driven by magnetostrictive actuators. *Precis. Eng. J. Int. Soc. Precis. Eng. Nanotechnol.* **2020**, *66*, 255–268. [[CrossRef](#)]
20. Yan, Y.; Santaniello, T.; Bettini, L.G.; Minnai, C.; Bellacicca, A.; Porotti, R.; Denti, I.; Faraone, G.; Merlini, M.; Lenardi, C.; et al. Electroactive ionic soft actuators with monolithically integrated gold nanocomposite electrodes. *Adv. Mater.* **2017**, *29*, 1606109:1–1606109:9. [[CrossRef](#)] [[PubMed](#)]
21. Tamagawa, H.; Okada, K.; Mulembo, T.; Sasaki, M.; Naito, K.; Nagai, G.; Nitta, T.; Yew, K.C.; Ikeda, K. Simultaneous enhancement of bending and blocking force of an ionic polymer-metal composite (IPMC) by the active use of its material characteristics change. *Actuators* **2019**, *8*, 29. [[CrossRef](#)]
22. Ma, S.; Zhang, Y.; Liang, Y.; Ren, L.; Tian, W.; Ren, L. High-performance ionic-polymer-metal composite: Toward large-deformation fast-response artificial muscles. *Adv. Funct. Mater.* **2019**, *30*, 1908508:1–1908508:9. [[CrossRef](#)]
23. Umrao, S.; Tabassian, R.; Kim, J.; Nguyen, V.H.; Zhou, Q.; Nam, S.; Oh, I.K. MXene artificial muscles based on ionically cross-linked  $Ti_3C_2T_x$  electrode for kinetic soft robotics. *Sci. Robot.* **2019**, *4*, eaaw7797:1–eaaw7797:11. [[CrossRef](#)] [[PubMed](#)]
24. Sun, Z.; Du, S.; Li, F.; Yang, L.; Zhang, D.; Song, W. High-performance cellulose based nanocomposite soft actuators with porous high-conductivity electrode doped by graphene-coated carbon nanosheet. *Cellulose* **2018**, *25*, 5807–5819. [[CrossRef](#)]
25. Wang, Y.; Liu, J.; Zhu, D.; Chen, H. Active tube-shaped actuator with embedded square rod-shaped ionic polymer-metal composites for robotic-assisted manipulation. *Appl. Bionics Biomech.* **2018**, *2018*, 4031705:1–4031705:12. [[CrossRef](#)]
26. Yu, M.; Shen, H.; Dai, Z. Manufacture and performance of ionic polymer-metal composites. *J. Bionic Eng.* **2007**, *4*, 143–149. [[CrossRef](#)]
27. Kim, K.J.; Shahinpoor, M. Ionic polymer-metal composites: II. Manufacturing techniques. *Smart Mater. Struct.* **2003**, *12*, 65–79. [[CrossRef](#)]
28. Li, S.L.; Kim, W.Y.; Cheng, T.H.; Oh, I.K. A helical ionic polymer-metal composite actuator for radius control of biomedical active stents. *Smart Mater. Struct.* **2011**, *20*, 035008:1–035008:8. [[CrossRef](#)]
29. Shahinpoor, M. Smart ionic polymer conductor composite materials as multifunctional distributed nanosensors, nanoactuators and artificial muscles. In Proceedings of the ASME International Mechanical Engineering Congress and Exposition, Orlando, FL, USA, 5–11 November 2005; pp. 485–489.
30. Feng, G.H.; Zhan, Z.H. A room-temperature processed parylene-patterned helical ionic polymer-metal composite spring actuator with selectable active region. *Smart Mater. Struct.* **2014**, *23*, 045002:1–045002:13. [[CrossRef](#)]
31. Wang, M.; Yu, M.; Lu, M.; He, Q.; Ji, K.; Liu, L. Effects of  $Cu^{2+}$  counter ions on the actuation performance of flexible ionic polymer metal composite actuators. *J. Bionic Eng.* **2018**, *15*, 1047–1056. [[CrossRef](#)]
32. Shahinpoor, M.; Kim, K.J. Ionic polymer-metal composites: I. Fundamentals. *Smart Mater. Struct.* **2001**, *10*, 819–833. [[CrossRef](#)]
33. Wang, F.; Li, Q.; Park, J.O.; Zheng, S.; Choi, E. Ultralow voltage high-performance bioartificial muscles based on ionically crosslinked polypyrrole-coated functional carboxylated bacterial cellulose for soft robots. *Adv. Funct. Mater.* **2020**, *31*, 2007749:1–2007749:10. [[CrossRef](#)]
34. He, Q.; Yu, M.; Li, Y.; Ding, Y.; Guo, D.; Dai, Z. Investigation of ionic polymer metal composite actuators loaded with various tetraethyl orthosilicate contents. *J. Bionic Eng.* **2012**, *9*, 75–83. [[CrossRef](#)]
35. Takeuchi, I.; Asaka, K.; Kiyohara, K.; Sugino, T.; Terasawa, N.; Mukai, K.; Shiraiishi, S. Electromechanical behavior of a fully plastic actuator based on dispersed nano-carbon/ionic-liquid-gel electrodes. *Carbon* **2009**, *47*, 1373–1380. [[CrossRef](#)]
36. Chen, Z.; Tan, X. A control-oriented and physics-based model for ionic polymer-metal composite actuators. *IEEE-ASME Trans. Mechatron.* **2008**, *13*, 519–529. [[CrossRef](#)]
37. He, Q.; Yu, M.; Song, L.; Ding, H.; Zhang, X.; Dai, Z. Experimental study and model analysis of the performance of IPMC membranes with various thickness. *J. Bionic Eng.* **2011**, *8*, 77–85. [[CrossRef](#)]
38. Shen, Q.; Palmre, V.; Stalbaum, T.; Kim, K.J. A comprehensive physics-based model encompassing variable surface resistance and underlying physics of ionic polymer-metal composite actuators. *J. Appl. Phys.* **2015**, *118*, 124904:1–124904:12. [[CrossRef](#)]
39. Vokoun, D.; He, Q.; Heller, L.; Yu, M.; Dai, Z. Modeling of IPMC cantilever's displacements and blocking forces. *J. Bionic Eng.* **2015**, *12*, 142–151. [[CrossRef](#)]
40. Tadokoro, S.; Yamagami, S.; Takamori, T.; Oguro, K. Modeling of Nafion-Pt composite actuators (ICPF) by ionic motion. In Proceedings of the Smart Structures and Materials 2000: Electroactive Polymer Actuators and Devices, Newport Beach, CA, USA, 5–9 March 2000; pp. 92–102. [[CrossRef](#)]
41. De Gennes, P.G.; Okumura, K.; Shahinpoor, M.; Kim, K.J. Mechanoelectric effects in ionic gels. *EPL* **2000**, *50*, 513–518. [[CrossRef](#)]
42. Nemat-Nasser, S.; Li, J.Y. Electromechanical response of ionic polymer-metal composites. *J. Appl. Phys.* **2000**, *87*, 3321–3331. [[CrossRef](#)]
43. Espinoza-Quinones, F.R.; Romani, M.; Borba, C.E.; Modenes, A.N.; Utzig, C.F.; Dall'Oglio, I.C. A mathematical approach based on the Nernst-Planck equation for the total electric voltage demanded by the electrocoagulation process: Effects of a time-dependent electrical conductivity. *Chem. Eng. Sci.* **2020**, *220*, 115626:1–115626:15. [[CrossRef](#)]

44. Zhang, Q.; Tu, B.; Fang, Q.; Lu, B. A structure-preserving finite element discretization for the time-dependent Nernst-Planck equation. *J. Appl. Math. Comput.* **2021**, 1–20. [[CrossRef](#)]
45. Warren, P.B. Non-faradaic electric currents in the Nernst-Planck equations and nonlocal diffusiophoresis of suspended colloids in crossed salt gradients. *Phys. Rev. Lett.* **2020**, *124*, 248004:1–248004:5. [[CrossRef](#)]
46. Chidiac, S.E.; Shafikhani, M. Electrical resistivity model for quantifying concrete chloride diffusion coefficient. *Cem. Concr. Compos.* **2020**, *113*, 103707:1–338414:12. [[CrossRef](#)]
47. Goona, N.K.; Parne, S.R.; Sashidhar, S. Distributed Source Scheme to solve the classical form of Poisson equation using 3-D Finite-Difference Method for improved accuracy and unrestricted source position. *Math. Comput. Simul.* **2021**, *190*, 965–975. [[CrossRef](#)]
48. Peng, H.; Hui, Y.; Ding, Q.; Li, H.; Zhao, C. IPMC gripper static analysis based on finite element analysis. *Front. Mech. Eng.* **2010**, *5*, 204–211. [[CrossRef](#)]